IAVS: A Multi-Center Dataset and Applicability Evaluation System for Computational Fluid Dynamics-Oriented Intracranial Aneurysm Segmentation

Feiyang Xiao[1,2†], Yichi Zhang[2,1†], Xigui Li[2,1†], Yuanye Zhou[3,1], Chen Jiang[2,1], Xin Guo[2,1], Limei Han[2,1], Yuxin Li[4], Fengping Zhu[4✉], and Yuan Cheng[2,1✉]

[1] Shanghai Academy of Artificial Intelligence for Science, Shanghai, China
[2] Artificial Intelligence Innovation and Incubation Institute, Fudan University, Shanghai, China
[3] University of Edinburgh, Edinburgh, UK
[4] Huashan Hospital, Fudan University, Shanghai, China
zhufengping@fudan.edu.cn, cheng_yuan@fudan.edu.cn

Abstract. The precise segmentation of intracranial aneurysms and their parent vessels (IA-Vessel) is a critical step for hemodynamic analyses, which primarily depend on Computational Fluid Dynamics (CFD). However, current segmentation methods predominantly focus on image-based evaluation metrics, often neglecting their practical effectiveness in subsequent CFD applications. Metrics such as the Dice similarity coefficient are insensitive to geometric topological abnormalities including vessel adhesion and surface irregularities which frequently cause CFD validation failures due to mesh generation errors or flow field distortions. To address these deficiencies, we construct an evaluation benchmark, the Intracranial Aneurysm Vessel Segmentation (IAVS) dataset, which is the first comprehensive, multi-center collection comprising 641 3D MRA images with 587 expert-verified annotations of aneurysms and IA-Vessels. In addition to image-mask pairs, the IAVS dataset provides standardized geometric files including STL models, vascular centerlines, and mesh grids alongside detailed hemodynamic analysis outcomes. Furthermore, we establish a standardized CFD applicability evaluation system that enables the automated and consistent conversion of segmentation masks into simulation-ready CFD models via a CFD conversion pipeline. Based on this system, we introduce a novel application-oriented metric, the CFD-Applicability Score (CFD-AS), to facilitate a comprehensive assessment of segmentation results focused on their clinical utility. The IAVS dataset and evaluation framework offer a robust foundation for bridging the gap between medical image segmentation and clinical hemodynamic research. The dataset, code, and model weights will be released after the paper is accepted.

Keywords: Intracranial Aneurysm Segmentation · Vessel Segmentation · Magnetic Resonance Angiography · Computational Fluid Dynamics

† These authors contributed equally.

1 Introduction

Intracranial aneurysms (IA) are pathological vascular dilations that risk enlarging and rupturing, causing high morbidity and mortality [16,2]. Assessing rupture risk is vital for clinical intervention [4], often relying on Computational Fluid Dynamics (CFD) to quantify hemodynamic parameters like wall shear stress [9,11,18]. Non-invasive Magnetic Resonance Angiography (MRA) is the standard for visualizing these complex structures [14]. Because manual delineation is labor-intensive [8], automated deep learning segmentation of IAs and parent vessels (IA-Vessel) is highly desirable for downstream CFD [13,6]. However, training such models requires robust, open-source datasets [1,5,7,10,15].

Despite existing IA datasets like ADAM [17] and Royal [12], significant translational gaps remain for hemodynamic analysis. First, they lack refined parent vessel annotations, geometric validation labels, and corresponding hemodynamic records, hindering end-to-end CFD modeling. Second, traditional evaluation relies on overlap-based metrics like the Dice coefficient, which are insensitive to topological abnormalities (e.g., vessel adhesion, surface irregularities). Such minute errors frequently cause mesh generation failures or flow field distortions during CFD validation. Furthermore, poor localization of small IAs and disrupted vascular connectivity severely impede the transition from image segmentation to biomechanical modeling. To bridge these gaps, we present a systematic solution for CFD-applicable IA and vessel segmentation. Our main contributions include:

- We collect and curate a large-scale multi-centre **I**ntracranial **A**neurysm **V**essel **S**egmentation (IAVS) dataset as an evaluation benchmark, comprising 641 3D MRA images and 587 annotations of aneurysms and IA-Vessels, including CFD analysis results. This dataset addresses the limitations of previous datasets that lack topological integrity and CFD applicability.
- We establish an standardised CFD applicability evaluation system that enables standardized estimation of CFD success probability given segmentation results. Additionally, we introduce a novel evaluation metric, the CFD-Applicability Score (CFD-AS), to facilitate a more comprehensive assessment of segmentation results.

2 IAVS Dataset

Motivation and Details. Existing intracranial aneurysm datasets have structural deficiencies in the annotation and lack applicability in CFD applications. To bridge this gap, our IAVS dataset contains 641 3D MRA images and 587 aneurysms and IA-Vessels annotations with CFD analysis results, which is adapted from three existing datasets including ADAM [17], INSTED [3] and Royal [12], and a new in-house dataset. An overview of IAVS dataset is shown in Figure 1. For public datasets, the original ADAM and INSTED datasets only provide annotations of IAs. Despite the Royal dataset contains IA-Vessel mask and STL models, several samples feature vessel adhesion and are not applicable for CFD analysis.

Table 1. Statistics of IAVS dataset including data source, number and diameter of IAs.

Dataset	No. of Images			No. of IAs per case				IAs	Diameter of IA		
	Total	Public	Private	0	1	2	≥3		<3mm	3-7mm	>7mm
Train	467	175	292	82	346	34	6	432	55	272	105
Set A	76	76	0	42	29	3	2	41	16	17	8
Set B	98	0	98	0	85	10	3	114	10	93	11

Table 2. Statistics of imaging parameters in the IAVS dataset.

Dataset Statistics	Min	Median	Max
Spacing (mm)	(0.21, 0.21, 0.30)	(0.36, 0.36, 0.50)	(0.47, 0.47, 1.20)
Volume Size (voxels)	(348, 384, 44)	(512, 512, 148)	(1024, 1024, 368)

In contrast, our dataset contains CFD applicable segmentation masks and CFD analysis results, including 3D MRA images (1), voxel-level segmentation masks (2)-(3), geometric models (4)-(6) and CFD analysis results (7). The IAVS dataset comprises 641 3D MRA images in total, containing 587 individual aneurysms with corresponding expert-verified annotations of both the aneurysms and their parent vessels (IA-Vessels). Among the 641 images, 124 are aneurysm-negative cases included; detailed statistics are provided in Table 1.

Data Statistics. The aneurysm quantity and size distribution in IAVS closely mirrors clinical epidemiological patterns, ensuring representativeness (Table 1). All data underwent strict anonymization and ethical approval. We partition the images into 467 cases for training/validation, 76 public cases as Set A (internal evaluation), and 98 private cases as Set B (clinical scenario evaluation). Specifically, Stage I (localization) uses 373/94 cases for training/validation, and Stage II (segmentation) uses 357/99 cropped patches respectively.

Annotation. After integrating the three public and private datasets, we conduct IA and IA-Vessel annotations for CFD-applicable segmentation (workflow in Figure 1). Existing IA annotations are used when available, while in-house data are annotated and checked by experienced radiologists. To annotate the parent vessels, we first apply a pre-trained COSTA model [12] (achieving a Dice of 0.9204 on its official test set) to preliminary segment the whole-brain vessels. Focusing on the aneurysm-related regions, these parent vessels are cropped from the coarse mask and subsequently refined and verified using 3D Slicer by a CFD specialist and a board-certified radiologist. This refinement process strictly adheres to clinical anatomical principles, eliminating abnormal geometric features and implementing an adaptive truncation strategy at vascular bifurcations. Specifically, if a parent vessel extends to a bifurcation and the branch length exceeds its diameter, truncation is performed. This strategy effectively avoids adhesion issues in distal small branches while ensuring the model can consistently learn vessel lengths.

Quality Control. To further validate the CFD usability of annotations, other than conducting voxel-level segmentation masks, all cases are conducted vascular

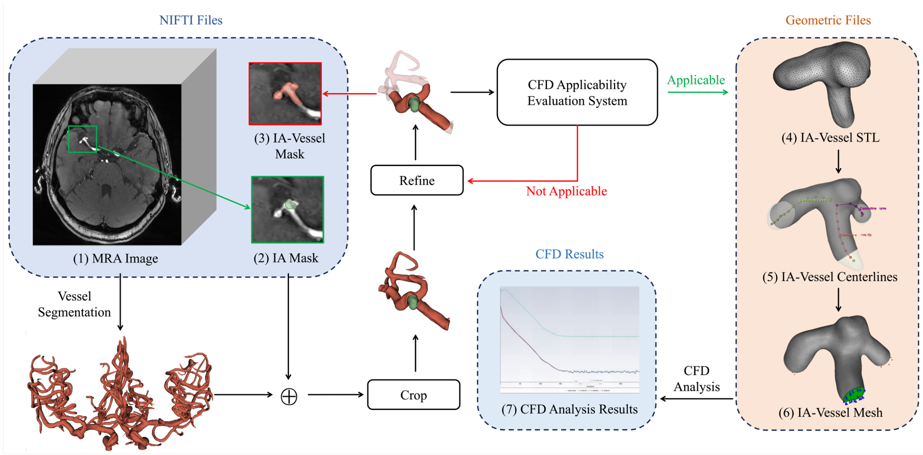

Fig. 1. An overview of the IAVS dataset and the annotation workflow. Each case encompasses seven types of standardized data: (1) whole-brain MRA images, (2) IA mask, (3) IA-Vessel mask, (4) STL models with cut inlets/outlets, (5) vascular centerlines, (6) mesh files with boundary annotations, (7) CFD analysis results.

geometric annotations for CFD analysis, including STL files of cut inlet/outlet sections, vascular centerline data, and mesh grid files labeled with fluid boundary conditions. Besides, CFD applicability of the segmentation masks are evaluated to validate whether the pressure and velocity residuals in the blood flow dynamics analysis achieve convergence. We perform a rigorous quality check and screening, annotations not applicable for CFD are further refined and validated, or removed from the final dataset.

3 CFD Applicability Evaluation System

To achieve automated and standardized conversion from segmentation mask to CFD model, we establish a standardised CFD applicability evaluation system as shown in Figure 2. The pipeline consists of the following steps, including vascular topology inspection, morphological preprocessing, geometric model conversion, centerline generation, end face cutting, mesh enhancement, surface fitting, boundary labeling, mesh generation, and CFD computation. The detailed steps are as follows:

Check Vessel Geometry. Vascular topology is first screened for geometric defects such as abnormal adhesions, holes, depressions, and protrusions. Discontinuities, holes, and partial adhesions are automatically identified by computing Betti numbers, which detect most topological anomalies. To further improve surface quality, 3D Slicer is employed to automatically fill remaining small holes, apply a median filter with a 1mm kernel for surface smoothing, and retain the largest connected component to exclude isolated noise. In approximately 1% of

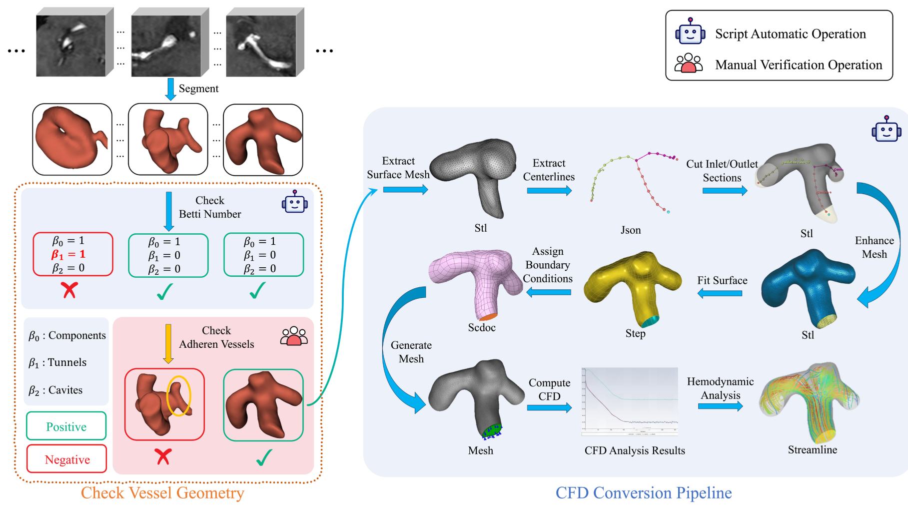

Fig. 2. Overview of our conversion pipeline from segmentation masks to CFD models, which realizes the entire chain process from medical imaging to flow field simulation. The pipeline consists of following steps, including vascular topology inspection, morphological preprocessing, geometric model conversion, centerline generation, end face cutting, mesh enhancement, surface fitting, boundary labeling, mesh generation, and CFD computation.

cases, over-smoothing may cause abnormal adhesion; these are manually corrected with the segmentation tools in 3D Slicer.

Extract Surface Mesh. First, the segmentation results are preprocessed. 3D Slicer is used to automatically fill small holes, apply a median filter with a kernel size of 1 mm for surface smoothing, and extract the largest connected component. Finally, the voxel-based NIFTI image data are converted into a 3D surface STL model, providing the geometric basis for subsequent CFD analysis.

Extract Centerlines. Based on the generated STL model, the VMTK toolkit is used to automatically identify the topological endpoints of vessel inlets and outlets and generate the corresponding vessel centerlines. A small number of cases show deviations in automatic detection and are corrected via manual interactive editing in 3D Slicer.

Cut Inlet/Outlet Sections. The ptvista library is used to cut vessel cross-sections according to the normal vectors of the centerlines. The cutting plane is uniformly set at 1/5 of the end segment position (when the radius at the candidate cut point is smaller than 0.3 mm, it automatically falls back to a proximal position that satisfies the radius requirement). Experiments show that about 10% of samples cannot be cut automatically due to insufficient centerline length and require manual intervention using Geomagic Wrap 2021.

Enhance Mesh. Geomagic Wrap is used to perform mesh optimization: first, Mesh Doctor repairs non-manifold edges, self-intersections, and highly skewed edges; then remeshing, refinement, optimization, and enhancement operations are performed. All parameters are set to the software defaults to ensure consistency of processing.

Fit Surface. The STL mesh file is reconstructed into a CAD model with precise geometric definitions and topological relationships, i.e., a STEP-format file. Surface patches are built based on the STL mesh, a mesh is generated, and the surface is fitted to produce the STEP file. The number of surface patches is set to 1000. At this stage, fewer than 1% of cases may detect intersecting meshes during mesh generation; this can be fixed manually by moving surface-patch vertices to eliminate concave polygons.

Assign Boundary Conditions. The STEP model is imported into ANSYS SpaceClaim to define boundary conditions, including accurate labeling of the inlet, outlet, wall, and fluid domain. End faces are automatically identified using the previously generated endpoint and centerline information, and the final model is saved in SCDOC format.

Generate Mesh. Fluent Meshing is used to generate an unstructured polyhedral mesh. Mesh quality and computational stability are ensured through CFL-number control and residual monitoring.

Compute CFD. Blood flow is simulated using an incompressible Newtonian fluid model. The icoFoam solver in Open Field Operation and Manipulation (OpenFOAM [19]) together with the PISO algorithm is used to solve the Navier–Stokes equations, computing velocity fields, pressure fields, and wall shear stress distributions over a mass flow rate range of 0.0010–0.0040 kg/s (steady-state simulations only).

Hemodynamic Analysis. Finally, the simulated flow field is visualized to generate velocity streamlines. These streamlines effectively reveal complex flow patterns within aneurysms, providing key biomechanical evidence for subsequent hemodynamic analysis and clinical risk assessment.

Based on the evaluation system, we propose a novel applicability-based evaluation metric entitled CFD applicability score (CFD-AS) to enable more comprehensive evaluation of segmentation results, which is defined as follows:

$$AS_{\mathrm{CFD}} = \frac{\widehat{TP}}{TP + FP + FN} \tag{1}$$

$$\widehat{TP} = \sum_{i=1}^{N} (y = 1) \wedge (\hat{y} = 1) \wedge (AE(\hat{y}) = 1) \tag{2}$$

$$AE_{\hat{y}} = \begin{cases} 1, & \text{if } (VTA_{\hat{y}}) = 1 \wedge (MGA_{\hat{y}}) = 1 \wedge (BFA_{\hat{y}}) = 1 \\ 0, & \text{if } (VTA_{\hat{y}}) = 0 \vee (MGA_{\hat{y}}) = 0 \vee (BFA_{\hat{y}}) = 0 \end{cases} \tag{3}$$

where $\widehat{TP}$ represents true positive cases that can be successfully applicable for CFD analysis. Specifically, $VTA_{\hat{y}} \in \{0, 1\}$, $MGA_{\hat{y}} \in \{0, 1\}$, and $BFA_{\hat{y}} \in \{0, 1\}$ represent the vascular topology availability, mesh generation availability, and blood flow availability of the segmentation mask $\hat{y}$, indicating, respectively,

Table 3. Comparison of different methods for aneurysm localization (Stage I).

Method	Set A			
	PR↑	**RE↑**	**ACC↑**	**F1↑**
nnDetection	0.3737 ± 0.4122	**0.9250** ± 0.4926	0.3627 ± 0.4131	0.5324 ± 0.4225
SwinUNETR	0.3472 ± 0.4718	0.6098 ± 0.5004	0.2841 ± 0.4644	0.4425 ± 0.4642
nnUNet	**0.5778** ± 0.4754	0.6341 ± 0.4853	**0.4333** ± 0.4668	**0.6047** ± 0.4650
Method	**Set B**			
	PR↑	**RE↑**	**ACC↑**	**F1↑**
nnDetection	0.5440 ± 0.3036	**0.9292** ± 0.1751	0.5224 ± 0.3017	0.6863 ± 0.2389
SwinUNETR	0.5145 ± 0.3956	0.7807 ± 0.3792	0.4495 ± 0.3884	0.6202 ± 0.3650
nnUNet	**0.6942** ± 0.4046	0.7368 ± 0.4033	**0.5563** ± 0.4008	**0.7149** ± 0.3846

Table 4. Evaluation of topological-aware loss for IA-Vessel segmentation (Stage II).

Model	Topological-aware Loss	Set A			
		Dice↑	**HD95↓**	**clDice↑**	**BIoU↑**
nnUNet	-	0.8533 ± 0.0840	**3.2187** ± 2.7283	0.8555 ± 0.1113	0.7527 ± 0.1211
nnUNet	clDice Loss	**0.8563** ± 0.0878	3.2809 ± 3.0868	**0.8629** ± 0.1175	**0.7576** ± 0.1214
Model	**Topological-aware Loss**	**Set B**			
		Dice↑	**HD95↓**	**clDice↑**	**BIoU↑**
nnUNet	-	0.8363 ± 0.1307	4.2557 ± 5.6929	0.8538 ± 0.1502	0.7368 ± 0.1652
nnUNet	clDice Loss	**0.8368** ± 0.1368	4.2134 ± 5.5734	**0.8616** ± 0.1524	**0.7388** ± 0.1693

whether there are geometric topological abnormalities in the vessels, whether geometric errors occur during the conversion process that interrupt subsequent operations, and whether the generated mesh file can be successfully used for CFD analysis. The computation of all three indices above can be automated via scripts. Here, VTA, MGA, and BFA are intermediate binary variables that encode the success or failure of three critical sub-steps in the CFD pipeline; they are not intended as stand-alone evaluation metrics. Tracking which of the three variables fails for a given predicted mask allows developers to pinpoint the specific geometric deficiency (topology defect, meshing failure, or flow-field divergence) that prevents a usable simulation.

4 Benchmark Evaluation

We establish a benchmark evaluating both aneurysm localization and IA-vessel segmentation. For localization (Table 3), nnDetection achieved high recall ($>$0.92) but suffered from excessive false positives. Conversely, nnUNet provided the best balance, achieving the highest F1-scores of 0.6047 (Set A) and 0.7149 (Set B). For segmentation (Table 4), integrating clDice loss into nnUNet marginally improved Dice scores but notably enhanced topology metrics (clDice and BIoU), confirming that topology-aware losses are essential for maintaining vascular connectivity and reducing structural errors.

Evaluation of CFD Applicability. Finally, we integrate the localization in Stage I with the segmentation in Stage II to enable end-to-end segmentation.

Table 5. Performance of different frameworks for end-to-end IA-Vessel segmentation.

Framework	Set A			
	Dice↑	**HD95↓**	**clDice↑**	**BIoU↑**
nnUNet Baseline	0.1548 ± 0.2520	48.8495 ± 39.9534	0.1552 ± 0.2468	0.1088 ± 0.1927
Stage I nnDetection + Stage II	0.4285 ± 0.3753	**15.9663** ± 17.8063	0.4311 ± 0.3862	0.3477 ± 0.3236
Stage I nnUNet + Stage II	**0.4864** ± 0.4070	50.5446 ± 90.9340	**0.4943** ± 0.4124	**0.4174** ± 0.3686
Stage I GT + Stage II	0.8563 ± 0.0878	3.2809 ± 3.0868	0.8629 ± 0.1175	0.7576 ± 0.1214
Framework	**Set B**			
	Dice↑	**HD95↓**	**clDice↑**	**BIoU↑**
nnUNet Baseline	0.4557 ± 0.2898	37.2055 ± 17.9024	0.4323 ± 0.2853	0.3395 ± 0.2496
Stage I nnDetection + Stage II	**0.6611** ± 0.2252	**19.6505** ± 17.8079	**0.6846** ± 0.2334	**0.5344** ± 0.2476
Stage I nnUNet + Stage II	0.6186 ± 0.3499	65.7056 ± 112.9016	0.6477 ± 0.3556	0.5286 ± 0.3264
Stage I GT + Stage II	0.8368 ± 0.1368	4.2134 ± 5.5734	0.8616 ± 0.1524	0.7388 ± 0.1693

In comparison, we conduct direct end-to-end IA-Vessel segmentation using the nnUNet as the baseline performance, and ground truth aneurysm localization for patch cropping as an upper-bound comparison. As shown in Table 5, direct end-to-end nnUNet segmentation yields Dice coefficients of 0.1548 on Set A and 0.4557 on Set B. Due to an excessive number of false positives over 120 and fewer than 10 true positives, we conclude that the direct end-to-end voxel-wise segmentation approach is highly susceptible to background noise and is not suitable for this specific task. Cascaded frameworks show improvements in conventional metrics. We uniformly set the Stage II model to the nnUNet with clDice Loss in the final evaluation of our proposed application-oriented metric AS_{CFD} in Table 6. We observe despite improvements in Dice coefficients using cascaded strategies, the state-of-the-art baselines struggle significantly to produce simulation-ready models. The best-performing baseline framework achieves an applicability score of only 38.33% on Set A and 43.05% on Set B. The majority of failure cases ($\widehat{TP}$ vs TP) are attributed to microscopic topological errors, such as spurious vessel connections and surface irregularities, which are largely ignored by volumetric overlap metrics but fatally disrupt the CFD conversion pipeline. These findings strongly validate the necessity of the IAVS dataset and the AS_{CFD} metric, highlighting a critical area for future optimization in medical image segmentation towards clinical utility. Analyzing the gap between the total true positives (TP) and the CFD-applicable subset ($\widehat{TP}$) reveals three dominant failure modes: (1) local vessel adhesion or small holes, which cause the topology check ($VTA = 0$) to fail; (2) excessive surface roughness that leads to mesh-generation errors ($MGA = 0$); and (3) a small number of cases where centerline extraction or boundary-condition assignment fails ($BFA = 0$). These defects are almost invisible to volume-overlap metrics such as Dice, further underscoring the necessity of the proposed CFD-AS.

5 Conclusion

In conclusion, we introduced the IAVS dataset and the novel CFD Applicability Score to bridge the translational gap between traditional image-based evaluation

Table 6. Evaluation of CFD Applicability Score of different IA-Vessel segmentation frameworks.

Framework	Set A					Set B				
	TP	**FP**	**FN**	$\widehat{TP}$	AS_{CFD}	**TP**	**FP**	**FN**	$\widehat{TP}$	AS_{CFD}
Stage I nnDetection + Stage II	37	62	4	30	29.13%	105	88	9	74	36.63%
Stage I nnUNet + Stage II	26	19	15	23	**38.33%**	84	37	30	65	**43.05%**
Stage I GT + Stage II	41	0	0	35	85.37%	114	0	0	88	77.19%
IA-Vessel GT	41	0	0	41	100.00%	114	0	0	114	100.00%

and clinical hemodynamic simulation. Our benchmark demonstrates a stark disparity between high volumetric overlap metrics and actual clinical feasibility, highlighting that even minor topological errors frequently cause simulation failures.

Disclosure of Interests

The authors have no competing interests to declare that are relevant to the content of this article.

References

1. Antonelli, M., Reinke, A., Bakas, S., Farahani, K., Kopp-Schneider, A., Landman, B.A., Litjens, G., Menze, B., Ronneberger, O., Summers, R.M., et al.: The medical segmentation decathlon. Nature communications **13**(1), 4128 (2022) 2
2. Cebral, J.R., Castro, M.A., Appanaboyina, S., Putman, C.M., Millan, D., Frangi, A.F.: Efficient pipeline for image-based patient-specific analysis of cerebral aneurysm hemodynamics: technique and sensitivity. IEEE transactions on medical imaging **24**(4), 457–467 (2005) 2
3. Chen, H., Zhao, X., Li, R., Li, H., Sun, H., Xu, Z., Wei, H., Li, Y., Dou, J., Li, X.: Intracranial aneurysm and intracranial artery stenosis detection and segmentation challenge (2024). https://doi.org/10.5281/zenodo.10990482, https://zenodo.org/records/10990482 2
4. Etminan, N., Rinkel, G.J.: Unruptured intracranial aneurysms: development, rupture and preventive management. Nature Reviews Neurology **12**(12), 699–713 (2016) 2
5. Gatidis, S., Hepp, T., Früh, M., La Fougère, C., Nikolaou, K., Pfannenberg, C., Schölkopf, B., Küstner, T., Cyran, C., Rubin, D.: A whole-body FDG-PET/CT dataset with manually annotated tumor lesions. Scientific Data **9**(1), 601 (2022) 2
6. Isensee, F., Jaeger, P.F., Kohl, S.A., Petersen, J., Maier-Hein, K.H.: nnU-Net: a self-configuring method for deep learning-based biomedical image segmentation. Nature methods **18**(2), 203–211 (2021) 2
7. Ji, Y., Bai, H., Ge, C., Yang, J., Zhu, Y., Zhang, R., Li, Z., Zhanng, L., Ma, W., Wan, X., et al.: Amos: A large-scale abdominal multi-organ benchmark for versatile medical image segmentation. Advances in neural information processing systems **35**, 36722–36732 (2022) 2

8. Jiao, R., Zhang, Y., Ding, L., Xue, B., Zhang, J., Cai, R., Jin, C.: Learning with limited annotations: a survey on deep semi-supervised learning for medical image segmentation. Computers in Biology and Medicine p. 107840 (2023) 2
9. Li, X., Zhou, Y., Xiao, F., Guo, X., Zhang, Y., Jiang, C., Ge, J., Wang, X., Wang, Q., Zhang, T., et al.: Aneumo: A large-scale comprehensive synthetic dataset of aneurysm hemodynamics. arXiv preprint arXiv:2501.09980 (2025) 2
10. Ma, J., Zhang, Y., Gu, S., Zhu, C., Ge, C., Zhang, Y., An, X., Wang, C., Wang, Q., Liu, X., Cao, S., Zhang, Q., Liu, S., Wang, Y., Li, Y., He, J., Yang, X.: AbdomenCT-1K: Is abdominal organ segmentation a solved problem? IEEE Transactions on Pattern Analysis and Machine Intelligence **44**(10), 6695–6714 (2022) 2
11. Morris, P.D., Narracott, A., von Tengg-Kobligk, H., Soto, D.A.S., Hsiao, S., Lungu, A., Evans, P., Bressloff, N.W., Lawford, P.V., Hose, D.R., et al.: Computational fluid dynamics modelling in cardiovascular medicine. Heart **102**(1), 18–28 (2016) 2
12. de Nys, C.M., Liang, E.S., Prior, M., Woodruff, M.A., Novak, J.I., Murphy, A.R., Li, Z., Winter, C.D., Allenby, M.C.: Royal brisbane TOFMRA intracranial aneurysm database (2024) 2, 3
13. Patel, T.R., Patel, A., Veeturi, S.S., Shah, M., Waqas, M., Monteiro, A., Baig, A.A., Pinter, N., Levy, E.I., Siddiqui, A.H., et al.: Evaluating a 3D deep learning pipeline for cerebral vessel and intracranial aneurysm segmentation from computed tomography angiography–digital subtraction angiography image pairs. Neurosurgical Focus **54**(6), E13 (2023) 2
14. Pierot, L., Portefaix, C., Rodriguez-Régent, C., Gallas, S., Meder, J.F., Oppenheim, C.: Role of MRA in the detection of intracranial aneurysm in the acute phase of subarachnoid hemorrhage. Journal of Neuroradiology **40**(3), 204–210 (2013) 2
15. Qu, C., Zhang, T., Qiao, H., Tang, Y., Yuille, A.L., Zhou, Z., et al.: Abdomenatlas-8k: Annotating 8,000 CT volumes for multi-organ segmentation in three weeks. Advances in Neural Information Processing Systems **36**, 36620–36636 (2023) 2
16. Schievink, W.I.: Intracranial aneurysms. New England Journal of Medicine **336**(1), 28–40 (1997) 2
17. Timmins, K.M., van der Schaaf, I.C., Bennink, E., Ruigrok, Y.M., An, X., Baumgartner, M., Bourdon, P., De Feo, R., Noto, T.D., Dubost, F., Fava-Sanches, A., Feng, X., Giroud, C., Group, I., Hu, M., Jaeger, P.F., Kaiponen, J., Klimont, M., Li, Y., Li, H., Lin, Y., Loehr, T., Ma, J., Maier-Hein, K.H., Marie, G., Menze, B., Richiardi, J., Rjiba, S., Shah, D., Shit, S., Tohka, J., Urruty, T., Walińska, U., Yang, X., Yang, Y., Yin, Y., Velthuis, B.K., Kuijf, H.J.: Comparing methods of detecting and segmenting unruptured intracranial aneurysms on TOF-MRAs: The ADAM challenge. NeuroImage **238**, 118216 (2021). https://doi.org/https://doi.org/10.1016/j.neuroimage.2021.118216, https://www.sciencedirect.com/science/article/pii/S1053811921004936 2
18. Wang, J., Liu, F., Ge, J., Sun, Y., Tang, Y., Liang, X., Zhao, Y., Yu, W., Wu, J., Lin, C., et al.: Nasal septum deviation correlates with asymmetry in parkinson's disease. medRxiv pp. 2025–02 (2025) 2
19. Weller, H.G., Tabor, G., Jasak, H., Fureby, C.: A tensorial approach to computational continuum mechanics using object-oriented techniques. Computers in physics **12**(6), 620–631 (1998) 6